

Strong Coupling of Microwave Photons to Antiferromagnetic Fluctuations in an Organic Magnet

Matthias Mergenthaler,^{1,2,*} Junjie Liu,¹ Jennifer J. Le Roy,¹ Natalia Ares,¹ Amber L. Thompson,³ Lapo Bogani,¹ Fernando Luis,⁴ Stephen J. Blundell,² Tom Lancaster,⁵ Arzhang Ardavan,² G. Andrew D. Briggs,¹ Peter J. Leek,² and Edward A. Laird^{1,†}

¹*Department of Materials, University of Oxford, Oxford OX1 3PH, United Kingdom*

²*Clarendon Laboratory, Department of Physics, University of Oxford, Oxford OX1 3PU, United Kingdom*

³*Chemical Crystallography, Chemistry Research Laboratory, University of Oxford, Oxford OX1 3TA, United Kingdom*

⁴*Instituto de Ciencia de Materiales de Aragón (CSIC-U. de Zaragoza), 50009 Zaragoza, Spain*

⁵*Durham University, Centre for Materials Physics, Department of Physics, Durham DH1 3LE, United Kingdom*

(Received 17 March 2017; published 2 October 2017)

Coupling between a crystal of di(phenyl)-(2,4,6-trinitrophenyl)iminoazanium radicals and a superconducting microwave resonator is investigated in a circuit quantum electrodynamics (circuit QED) architecture. The crystal exhibits paramagnetic behavior above 4 K, with antiferromagnetic correlations appearing below this temperature, and we demonstrate strong coupling at base temperature. The magnetic resonance acquires a field angle dependence as the crystal is cooled down, indicating anisotropy of the exchange interactions. These results show that multispin modes in organic crystals are suitable for circuit QED, offering a platform for their coherent manipulation. They also utilize the circuit QED architecture as a way to probe spin correlations at low temperature.

DOI: 10.1103/PhysRevLett.119.147701

Hybrid circuit quantum electrodynamics (circuit QED) using spin ensembles coupled to microwave resonators [1–7] has potential use in quantum memories [8,9] as well as for microwave-to-optical conversion [10]. The first demonstrations used paramagnetic ensembles, but correlated states such as ferrimagnets lead to stronger coupling because of their high spin density [11,12]. However, this comes at the price of on-chip magnetic fields, to which both superconducting qubits (used as processors) and SQUID arrays (used for cavity tuning) are sensitive. Antiferromagnetic spin ensembles circumvent this obstacle by combining high spin densities with no net magnetization. Perpendicular spin axis alignments of antiferromagnetic domains can also be used as a classical memory, which is robust against high magnetic fields, invisible to magnetic sensors, and can be packed with high density. Antiferromagnetic memory devices can be manipulated and read out via electrical currents [13,14]. Furthermore, antiferromagnetic heterostructures would combine spintronic and magnonic functionalities [15]. Harnessing these possibilities makes it necessary to understand the range of interactions that occur in antiferromagnetic systems. As model systems, organic magnets can be engineered chemically to create well-defined magnetic interactions [16,17], which could be probed via circuit QED to test models of magnetism in different dimensions [18]. Characteristic interaction strengths in organic magnets are such that these materials typically approach or undergo a phase transition only at mK temperatures [19–22], making them difficult to study with conventional electron spin resonance (ESR).

Strong coupling to antiferromagnetic correlations, which has not yet been achieved in the circuit QED architecture, would allow these materials to be studied at low temperatures, low microwave frequencies, and low magnetic fields.

Here we demonstrate strong coupling between microwave modes of a superconducting resonator and a crystallized organic radical, di(phenyl)-(2,4,6-trinitrophenyl)iminoazanium (DPPH). In this material antiferromagnetic correlations become evident in spin resonance at a temperature $T \sim 4$ K and below, although no magnetic ordering is observed down to a temperature of 16 mK [23]. We measure coupling both to spin excitations (in the paramagnetic phase at high temperature $T \gtrsim 4$ K), and to excitations showing antiferromagnetic correlations at lower temperature [33,34]. By studying the angle dependence of the magnetic resonance, we investigate the anisotropy of the exchange interactions, evident from a separation of parallel and perpendicular resonances as the crystal is cooled. We measure the ensemble coupling as a function of temperature, which shows paramagnetic behavior above $T \sim 500$ mK but becomes temperature independent below $T \sim 50$ mK. The spin modes deviate from paramagnetic behavior due to antiferromagnetic (AFM) fluctuations being present, despite being above the AFM phase transition temperature.

To fabricate the superconducting resonator, a 110 nm NbTiN film was sputtered onto a quartz substrate, and patterned using optical lithography and reactive ion etching. The measured resonator (Fig. 1) has a signal line width of $w = 50 \mu\text{m}$ and a separation of $s = 5.3 \mu\text{m}$ from the lateral ground planes for 50Ω impedance matching. Single

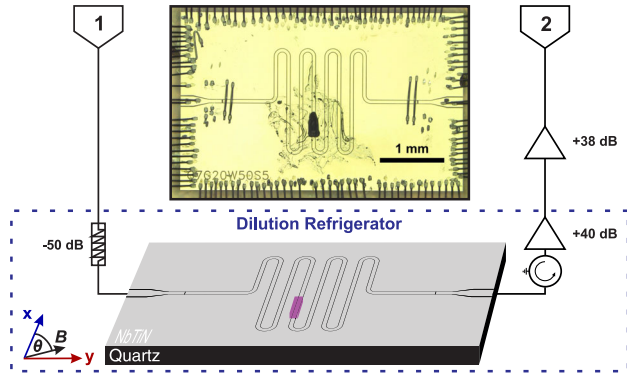


FIG. 1. Experimental schematic. The coplanar resonator (inset photograph) is mounted in a dilution refrigerator and measured via two-port microwave transmission. A DPPH crystal (purple in schematic, black in photograph) is attached with vacuum grease near the magnetic field antinode of the resonator's fundamental mode. Axes of the in-plane static magnetic field are indicated.

crystals were grown via a saturated solution of DPPH in toluene, sitting in a hexane bath at 5°C over two weeks. Using this method DPPH crystallizes in a triclinic P-1 space group with a unit cell consisting of four DPPH, one hexane, and one toluene molecule [23]. The largest crystals from two identically prepared growth batches were measured; results from one crystal (crystal I) are presented here, while results from crystal II, with similar behavior, are shown in the Supplemental Material [23]. Each measured crystal was attached near the magnetic field antinode of the cavity fundamental mode, with the long axis aligned along the CPWR, defining the x axis. Measurements were performed in a dilution refrigerator in an in-plane magnetic field $\mathbf{B} \equiv (B_x, B_y, 0)$.

The device was measured by transmission spectroscopy using a microwave network analyzer. In zero magnetic field and at $T = 15$ mK, the resonator (with crystal attached) exhibits a fundamental mode at frequency $\omega_0/2\pi = f_0 = 5.92$ GHz and a loaded quality factor of $Q_L = 1.51 \times 10^4$ [23]. An external magnetic field of magnitude $B \equiv |\mathbf{B}| = 165$ mT applied along x (along y) reduces this to $Q_L = 1.17 \times 10^4$ ($Q_L = 1.04 \times 10^4$).

To probe coupling to the crystal, the resonator transmission $|S_{21}|^2$ is measured at two different temperatures as a function of frequency f and magnetic field (Fig. 2). The bare cavity mode is evident as a transmission peak that is nearly field independent. As the magnetic field is swept, the spin resonance frequency f_{SR} is tuned through degeneracy with the cavity frequency $\omega_r/2\pi = f_r$, giving rise to an anticrossing when $f_{SR} \approx f_r$.

Because of the large number of molecular spins, it is appropriate to parametrize the coupling to the resonator by an effective ensemble coupling g_{eff} [1,4,35]. To extract g_{eff} , the system is modeled as two coupled oscillators, giving for the hybridized resonance frequency [36]

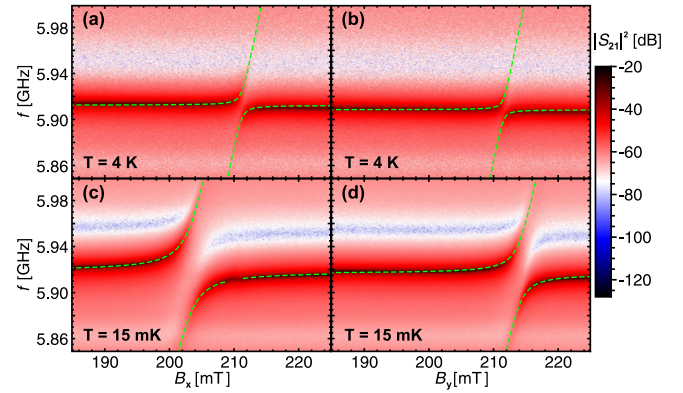


FIG. 2. Transmission as a function of external magnetic field $B_{x,y}$ and resonator probe frequency f , measured at two different temperatures. Transmission maxima occur at resonance frequencies of the combined system, with anticrossings indicating hybridization between crystal magnetic resonances and the cavity modes. Superimposed on each panel are fits to the resonance frequencies (dashed lines) using Eq. (1).

$$\omega_{\pm} = \omega_r + \frac{\Delta}{2} \pm \frac{1}{2} \sqrt{\Delta^2 + 4g_{\text{eff}}^2}, \quad (1)$$

where $\omega_{\pm}/2\pi = f_{\pm}$, $\Delta = g\mu_B(B_{x,y} - B_{\text{MR}})/\hbar$ is the frequency detuning and B_{MR} is the magnetic resonance (MR) field. Fitting the transmission peak locations in Fig. 2 to Eq. (1) and assuming a fixed Landé factor $g = 2.0037$ [37] gives the fit parameters g_{eff} and B_{MR} shown in Table I for the two field directions and temperatures.

The spin dephasing rate $\gamma(T)$ is deduced by fitting a standard input-output model [11,35,36,38,39]

$$|S_{21}(\omega)|^2 = \left| \frac{\kappa_c}{i(\omega - \omega_r) - \kappa + \frac{g_{\text{eff}}^2}{i(\omega - \omega_{\text{MR}}) - \gamma}} \right|^2, \quad (2)$$

where κ_c is the coupling rate to the external microwave circuit and $2\kappa/2\pi \equiv f_0/Q_L$ is the total relaxation rate of the resonator. We use Eq. (2) to fit $|S_{21}(\omega)|^2$ at the resonance fields B_{MR} , taking κ_c and γ as fit parameters and holding constant the parameters g_{eff} , ω_r and κ deduced above. Extracted values of γ are shown in Table I.

A dimensionless measure of the coupling efficiency is the cooperativity $C \equiv g_{\text{eff}}^2/\kappa\gamma$. We extract this parameter for each temperature and field axis (Table I). Already at

TABLE I. Resonance parameters extracted from Fig. 2 for different temperatures and magnetic field orientations.

T (K)	Axis	B_{MR} (mT)	$g_{\text{eff}}/2\pi$ (MHz)	$\gamma/2\pi$ (MHz)	C
4	x	211.19 ± 0.05	12.1 ± 0.4	15.0 ± 0.2	18
4	y	211.53 ± 0.05	9.6 ± 0.3	15.0 ± 0.2	10
0.015	x	203.12 ± 0.02	38.7 ± 0.1	29.6 ± 0.2	200
0.015	y	213.75 ± 0.05	26.9 ± 0.3	25.5 ± 0.4	102

$T = 4$ K, the system is in the regime of high cooperativity ($C > 1$), implying coherent transfer of excitations from the microwave field to the ensemble, while at $T = 15$ mK the strong coupling condition $g_{\text{eff}} \gg \kappa, \gamma$ is reached for \mathbf{B} along x , where the ensemble coupling is faster than the decay of both the spin ensemble and the cavity.

We now show that the crystal exhibits antiferromagnetic correlations at low temperature. Whereas at high temperature [Figs. 2(a) and 2(b)], the anticrossing field B_{MR} is nearly independent of angle, at $T = 15$ mK there is a pronounced anisotropy [Figs. 2(c) and 2(d)]. This is explored further in Fig. 3(a), which compares the dependence of B_{MR} on field angle θ at $T = 6$ K and $T = 15$ mK. Measuring near the fundamental cavity mode f_0 , the angle dependence is well fit by $B_{\text{MR}} = B_{\text{MR}}^{\text{offset}} + \Delta B_i \sin^2(\theta + \Delta\theta)$, with offsets $B_{\text{MR}}^{\text{offset}}$ and $\Delta\theta$ together with anisotropy ΔB_i as fit parameters, where $i \in \{0, 1\}$ labels the cavity mode. At low temperature, we find $\Delta B_0 = 10.6$ mT, whereas at 6 K there is almost no angle dependence.

At high temperature, this is consistent with a paramagnet with nearly isotropic g factor [23]. Anisotropy at lower temperature could arise from field screening by the superconductor, from temperature-dependent g -factor anisotropy, from trapped flux in the magnet coils, or from a transition to magnetic correlations in the crystal. Field screening is excluded by measurements with different crystal orientation [23]. To exclude g -factor anisotropy, we repeated the measurement at the first harmonic of the resonator [$f_1 = 11.64$ GHz, upper trace in Fig. 3(b)]. Whereas g -factor anisotropy would lead to $\Delta B_1 = 2\Delta B_0$, in fact we find $\Delta B_1 = 12.3$ mT $\approx \Delta B_0$. Trapped flux in the coils is also excluded by the temperature dependence, since the coils are thermally isolated from the sample. We therefore deduce an onset of AFM correlations between 15 mK and 4 K.

To confirm antiferromagnetic behavior, we plot the magnetic resonance dispersion relation for the two principal axes [Fig. 3(b)]. Although each branch contains only two data points, they clearly do not satisfy a paramagnetic (PM) dispersion relation $f = g\mu_B B_{\text{MR}}/h$ (dotted/dashed/dot-dashed lines on figure), even allowing for g -tensor anisotropy. However, they are well fit by an AFM dispersion relation [40] derived from a two-sublattice model with a molecular-field approximation at zero temperature [41]:

$$f = \frac{g\mu_B}{h} \sqrt{B_{\text{MR}}^2 \pm K}, \quad (3)$$

with the $+$ ($-$) branches describing field alignment parallel (perpendicular) to the anisotropy axis. Here the fit parameters are K , which parametrizes the exchange and anisotropy field of the crystal and separate g_x and g_y for the two field directions [40,42]. Fitting all four data points simultaneously, the best fit parameters are $K = 0.0014$ mT², $g_x = 2.04$, and $g_y = 1.99$, similar to a previously reported value $g = 2.0037$ in the PM phase [37]. At low temperature, the magnetic resonance excitations are no longer single spin flips, but antiferromagnetic fluctuations.

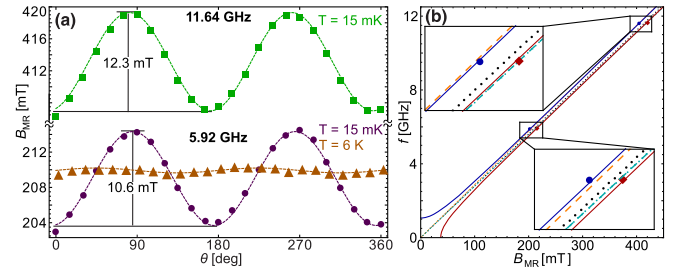


FIG. 3. (a) Resonance magnetic field as a function of field angle θ . Measuring at $T = 15$ mK, the resonance field varies sinusoidally with θ , with amplitude $\Delta B_0 = 10.6$ mT for the fundamental mode ($f_0 = 5.92$ GHz, circles) and $\Delta B_1 = 12.3$ mT for the first harmonic mode ($f_1 = 11.64$ GHz, squares). At high temperature, the fundamental mode shows nearly isotropic resonance (triangles). (b) Plot of the MR frequency as a function of resonance magnetic field. Data points are the resonance magnetic fields along x (circles) and along y (diamonds), taken from the maximum and minimum data points of (a) for data at the fundamental or first harmonic mode. The black dotted line is the PM dispersion relation with Landé factor $g = 2.0037$. The dashed orange and dot-dashed cyan lines are fits using a PM dispersion relation, with separate g factors along the two axes taken as fit parameters. From the insets it is apparent that these fits do not describe the data well. Red and blue solid curves are a fit to the AFM dispersion relation in Eq. (3), which agrees well with the data.

The temperature evolution of the effective polarization can be studied via the coupling strength g_{eff} [Fig. 4(a)]. Above 50 mK, g_{eff} decreases with increasing temperature, as expected from thermal depolarization of the spin ensemble. For a paramagnet, the effective coupling is [1]

$$g_{\text{eff}}(T) = g_s \sqrt{N_p(T)} = g_s \sqrt{N \tanh(hf/2k_B T)}, \quad (4)$$

where g_s is the root-mean-square coupling per individual spin and $N_p(T)$ is the net number of polarized spins out of N coupled radicals. Above $T = 0.5$ K [shaded region of Fig. 4(a)], Eq. (4) gives a good fit to the data; calculating $g_s/2\pi = 5$ Hz from the geometry of the resonator and taking the number of coupled radicals as a fit parameter gives $N_x = 1.5 \times 10^{14}$ for \mathbf{B} along x . This is in fair agreement with $N = 1.7 \times 10^{14}$ estimated from the geometry of the crystal. The data for \mathbf{B} along y give a smaller value $N_y = 7.1 \times 10^{13}$, as expected from the smaller perpendicular overlap with the alternating cavity field. High cooperativity ($C > 1$) is already reached far above base temperature, for example at $T = 0.5$ K, where $C_x = 66$ and $C_y = 28$. The agreement with the two-level model [Eq. (4)] confirms that the magnetic resonance spectroscopy probes a transition from the spin ground state (rather than between two excited states).

Below 0.5 K, g_{eff} is found to be smaller than the fits would predict. This may reflect screening of each spin by its neighbors as the antiferromagnetic phase is approached (although the $\sqrt{N_p}$ enhancement of g_{eff} is still expected

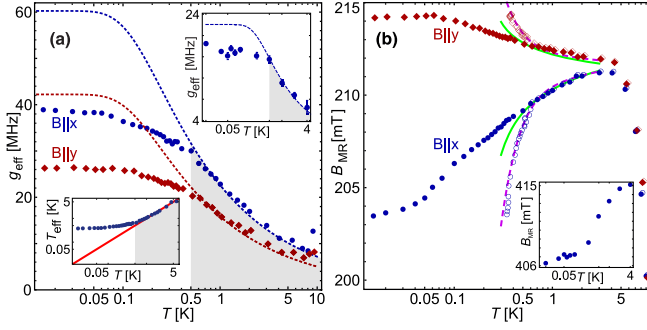


FIG. 4. (a) Temperature evolution of g_{eff} for \mathbf{B} applied along x and y . Above $T \sim 500$ mK, the data agree with a PM model [dashed lines, fit to Eq. (4) over the shaded temperature range]. Inset right: similar data and fits at the resonator's first harmonic. Inset left: effective spin-temperature calculated with Eq. (4) (points). (b) Filled symbols: resonance magnetic field along x and y as a function of temperature. As temperature decreases, the resonance magnetic field moves away from its paramagnetic value (assuming $g = 2.0037$). At intermediate temperatures, both branches are fit by a spin chain model (solid curves; see text). Unfilled symbols: B_{MR} along x and y as a function of effective temperature according to Eq. (4). The data for $T \leq 3$ K is fit by a spin chain model (dashed curve; see text). Inset: similar data at the first harmonic mode.

to apply [12]). It may also reflect a failure of the spin ensemble to thermalize. By comparing the measured $g_{\text{eff}}(T)$ with the value predicted by Eq. (4), an effective spin temperature T_{eff} can be extracted [Fig. 4(a) inset left]. At the lowest temperature, the effective number of coupled spins is $N_{\text{P}} = (g_{\text{eff}}/g_s)^2 \approx 5.9 \times 10^{13}$ for \mathbf{B} along x . Similar behavior is observed at the resonator's first harmonic mode [Fig. 4(a) inset right], with smaller overall coupling because the crystal is not located at a field antinode.

We now study the temperature dependence of the magnetic resonance, which gives experimental insight into the spin correlations, where analytical solutions for models of interacting spins in three dimensions do not exist. The shift of the magnetic resonance frequency away from the high-temperature (paramagnetic) value is a measure of short-range correlations. Filled symbols in Fig. 4(b) show the magnetic resonance field as a function of cryostat temperature for parallel and perpendicular field alignment. Both data sets exhibit a kink at $T \sim 50$ mK which could suggest a phase transition, and indeed such a transition to an AFM state at $T \sim 0.3$ K has been previously observed in DPPH [33,34]. However, in our sample, separate investigations using ac susceptibility and muon spectroscopy [23] show that there is no phase transition down to $T = 16$ mK. The transition temperature in DPPH is known to vary widely depending on the crystallizing solvent [43], and the incorporated toluene and hexane in our crystal presumably inhibits ordering at accessible temperatures [23]. For this reason, we attribute the low-temperature kink in Fig. 4(b) (filled symbols) to the failure of the spins to thermalize inside the resonator. This interpretation is supported by plotting the same data as a function of the

spin temperature T_{eff} [extracted as in Fig. 4(a) left inset], which shows that the kink disappears [Fig. 4(b), unfilled symbols]. At high temperature ($T \gtrsim 5$ K), the resonances shift to lower field because of the (independently measured) decrease in cavity frequency due to kinetic inductance.

The temperature dependence of the resonance frequencies is simulated by calculating the short range spin-spin correlations between DPPH molecules. The spin Hamiltonian is

$$\mathcal{H} = \mathcal{H}^0 + \mathcal{H}', \quad (5)$$

where $\mathcal{H}^0 = -2\sum_{i,j} J_{ij} \mathbf{S}_i \cdot \mathbf{S}_j - g\mu_B \sum_i \mathbf{B} \cdot \mathbf{S}_i$ incorporates isotropic exchange and Zeeman energy, and \mathcal{H}' represents the anisotropic exchange between molecules, e.g. dipole-dipole interactions. Here $\mathbf{S}_i = \{S_i^x, S_i^y, S_i^z\}$ is the spin of the i th molecule, and $J_{ij} < 0$ is the isotropic exchange. Equation (5) assumes an isotropic g tensor, which is not required by symmetry but is justified experimentally by the isotropy of the magnetic resonance field well above the phase transition [Fig. 3(a)]. We neglect the bulk permeability of the material. In the absence of anisotropy ($\mathcal{H}' = 0$), Eq. (5) leads to a temperature independent ESR resonance frequency with $f = g\mu_B B$, which is identical to the ESR resonance for noninteracting spins, despite the isotropic interaction [44]. Any shift of this resonance frequency indicates an effect of \mathcal{H}' . Assuming $\mathcal{H}^0 \gg \mathcal{H}'$, the frequency shift is [44–46]

$$h\delta f = -\frac{\langle [[\mathcal{H}', S^+], S^-] \rangle}{2\langle S^z \rangle}, \quad (6)$$

where $\langle \dots \rangle$ indicates the temperature-dependent expectation value, $\mathbf{S} \equiv \sum_i \mathbf{S}_i$ is the total spin operator, and $S^\pm \equiv S^x \pm iS^y$.

To gain insight into the role of antiferromagnetic fluctuations, we employ a simple model of a one-dimensional uniaxial anisotropic antiferromagnet [45]. This is also suggested by the crystal packing, where solvent molecules may act as blocks between chains [23]. We therefore have $\mathcal{H}^0 = -2J\sum_i \mathbf{S}_i \cdot \mathbf{S}_{i+1} - g\mu_B \sum_i \mathbf{B} \cdot \mathbf{S}_i$ and $\mathcal{H}' = 2J^A \sum_i S_i^x S_{i+1}^x$. In a classical approximation, expected to be valid at high temperature, the frequency shift Eq. (6) can be evaluated exactly [23,45,47]. With the exchange constants as free parameters, the shift along the x axis is fitted in the range $0.5 \text{ K} \leq T \leq 3 \text{ K}$, giving $J/k_B \sim -300 \pm 200$ mK and $J^A/k_B \sim -9 \pm 4$ mK [Fig. 4(b) lower solid curve]. The same parameters give a good match for the shift along the y axis [Fig. 4(b) upper solid curve].

As an alternative to fitting over this restricted temperature range, the data can also be fitted as a function of effective spin temperature T_{eff} over the entire range $T_{\text{eff}} \leq 3$ K [lower dashed curve in Fig. 4(b)]. This yields similar values $J/k_B = -1200 \pm 500$ mK and $J^A/k_B = -10 \pm 3$ mK. As before the same parameters give a good fit for the shift along y [Fig. 4(b) upper dashed curve]. Interestingly, in both cases the extracted anisotropic exchange is close to the

dipole-dipole interaction $J^A/k_B = -3\mu_0 g^2 \mu_B^2 / 8\pi a^3 k_B \sim -10$ mK estimated from the molecular spacing $a \sim 7.1$ Å. The deviation between fit and data presumably reflects the increasing importance of quantum correlations at low temperature and higher dimensionality of the interactions, neither of which is well captured by this one-dimensional model. The anisotropy axis in spin resonance coincides with the long axis of the crystal (the x axis) but does not appear to correspond to any preferred direction in the x-ray diffraction structure [23]. The temperature dependence does not simply result from a demagnetizing field, which would be weaker and would have the same sign for both orientations.

In conclusion, we have shown coupling between a microwave cavity and the molecular ensemble both in an uncorrelated and AFM correlated state [4,35]. This crystal structure presumably exhibits a complex network of exchange interactions, but these circuit QED spin resonance techniques, applied in future experiments, will enable measurements of spin systems with engineered interactions, for example, molecular magnets in one-dimensional chains or higher-dimensional systems with well-defined exchange pathways [16,17]. Magnetic resonance measurements on these molecules offer a way to extract spin correlation functions experimentally via Eq. (6), thereby offering a platform to test theoretical predictions for quantum correlated systems. As a quantum memory, organic magnetic ensembles offer a high spin density, and therefore a strong ensemble coupling, with potential for chemical engineering of the spin system.

We acknowledge L. P. Kouwenhoven for use of the sputterer, C. Baines, B. Huddart, M. Worsdale, and F. Xiao for experimental assistance with muon measurements made at the Swiss Muon Source (Paul Scherrer Institut, Switzerland), S. C. Speller for discussions, and support from EPSRC (EP/J015067/1 and EP/J001821/1), Marie Curie (CIG, IEF, and IIF), the ERC (338258 “OptoQMol”), Grant No. MAT2015-68204-R from Spanish MINECO, a Glasstone Fellowship, the Royal Society, the Royal Academy of Engineering, and Templeton World Charity Foundation. M. M. acknowledges support from the Stiftung der Deutschen Wirtschaft (sdw).

*matthias.mergenthaler@materials.ox.ac.uk

†edward.laird@materials.ox.ac.uk

- [1] J. H. Wesenberg, A. Ardavan, G. A. D. Briggs, J. J. L. Morton, R. J. Schoelkopf, D. I. Schuster, and K. Mølmer, *Phys. Rev. Lett.* **103**, 070502 (2009).
- [2] Z.-L. Xiang, S. Ashhab, J. You, and F. Nori, *Rev. Mod. Phys.* **85**, 623 (2013).
- [3] D. I. Schuster, A. Fragner, M. I. Dykman, S. A. Lyon, and R. J. Schoelkopf, *Phys. Rev. Lett.* **105**, 040503 (2010).
- [4] Y. Kubo, F. R. Ong, P. Bertet, D. Vion, V. Jacques, D. Zheng, A. Dréau, J.-F. Roch, A. Auffeves, F. Jelezko, J. Wrachtrup, M. F. Barthe, P. Bergonzo, and D. Esteve, *Phys. Rev. Lett.* **105**, 140502 (2010).
- [5] R. Amsüss, C. Koller, T. Nöbauer, S. Putz, S. Rotter, K. Sandner, S. Schneider, M. Schramböck, G. Steinhauser, H. Ritsch, J. Schmiedmayer, and J. Majer, *Phys. Rev. Lett.* **107**, 060502 (2011).
- [6] V. Ranjan, G. de Lange, R. Schutjens, T. Debelhoir, J. P. Groen, D. Szombati, D. J. Thoen, T. M. Klapwijk, R. Hanson, and L. DiCarlo, *Phys. Rev. Lett.* **110**, 067004 (2013).
- [7] C. Clauss, D. Bothner, D. Koelle, R. Kleiner, L. Bogani, M. Scheffler, and M. Dressel, *Appl. Phys. Lett.* **102**, 162601 (2013).
- [8] Y. Kubo, C. Grezes, A. Dewes, T. Umeda, J. Isoya, H. Sumiya, N. Morishita, H. Abe, S. Onoda, T. Ohshima, V. Jacques, A. Dréau, J.-F. Roch, I. Diniz, A. Auffeves, D. Vion, D. Esteve, and P. Bertet, *Phys. Rev. Lett.* **107**, 220501 (2011).
- [9] C. Grezes, B. Julsgaard, Y. Kubo, W. L. Ma, M. Stern, A. Bienfait, K. Nakamura, J. Isoya, S. Onoda, T. Ohshima, V. Jacques, D. Vion, D. Esteve, R. B. Liu, K. Mølmer, and P. Bertet, *Phys. Rev. A* **92**, 020301 (2015).
- [10] S. Blum, C. O’Brien, N. Lauk, P. Bushev, M. Fleischhauer, and G. Morigi, *Phys. Rev. A* **91**, 033834 (2015).
- [11] H. Huebl, C. W. Zollitsch, J. Lotze, F. Hocke, M. Greifenstein, A. Marx, R. Gross, and S. T. B. Goennenwein, *Phys. Rev. Lett.* **111**, 127003 (2013).
- [12] Y. Cao, P. Yan, H. Huebl, S. T. B. Goennenwein, and G. E. W. Bauer, *Phys. Rev. B* **91**, 094423 (2015).
- [13] X. Marti, I. Fina, C. Frontera, J. Liu, P. Wadley, Q. He, R. J. Paull, J. D. Clarkson, J. Kudrnovský, I. Turek, J. Kuneš, D. Yi, J.-H. Chu, C. T. Nelson, L. You, E. Arenholz, S. Salahuddin, J. Fontcuberta, T. Jungwirth, and R. Ramesh, *Nat. Mater.* **13**, 367 (2014).
- [14] T. Jungwirth, X. Marti, P. Wadley, and J. Wunderlich, *Nat. Nanotechnol.* **11**, 231 (2016).
- [15] R. E. Troncoso, C. Ulloa, F. Pesce, and A. S. Nunez, *Phys. Rev. B* **92**, 224424 (2015).
- [16] P. A. Goddard, J. L. Manson, J. Singleton, I. Franke, T. Lancaster, A. J. Steele, S. J. Blundell, C. Baines, F. L. Pratt, R. D. McDonald, O. E. Ayala-Valenzuela, J. F. Corbey, H. I. Southerland, P. Sengupta, and J. A. Schlueter, *Phys. Rev. Lett.* **108**, 077208 (2012).
- [17] J. Liu, P. A. Goddard, J. Singleton, J. Brambleby, F. Foronda, J. S. Möller, Y. Kohama, S. Ghannadzadeh, A. Ardavan, S. J. Blundell, T. Lancaster, F. Xiao, R. C. Williams, F. L. Pratt, P. J. Baker, K. Wierschem, S. H. Lapidus, K. H. Stone, P. W. Stephens, J. Bendix, T. J. Woods, K. E. Carreiro, H. E. Tran, C. J. Villa, and J. L. Manson, *Inorg. Chem.* **55**, 3515 (2016).
- [18] O. Kahn, *Molecular Magnetism* (VCH, New York, NY, 1993).
- [19] R. Chiarelli, M. A. Novak, A. Rassat, and J. L. Tholence, *Nature (London)* **363**, 147 (1993).
- [20] J. Sichelschmidt, V. A. Ivashin, J. Ferstl, C. Geibel, and F. Steglich, *Phys. Rev. Lett.* **91**, 156401 (2003).
- [21] S. J. Blundell and F. L. Pratt, *J. Phys. Condens. Matter* **16**, R771 (2004).
- [22] Y. Wiemann, J. Simmendinger, C. Clauss, L. Bogani, D. Bothner, D. Koelle, R. Kleiner, M. Dressel, and M. Scheffler, *Appl. Phys. Lett.* **106**, 193505 (2015).
- [23] See Supplemental Material at <http://link.aps.org/supplemental/10.1103/PhysRevLett.119.147701>, which includes Refs. [24–32], for resonator characterization, crystal

- characterization, susceptibility measurements, muon spectroscopy, data set of Crystal II and calculations of the temperature-dependent frequency shift, the single spin coupling, and number of radicals in the crystal.
- [24] A. Altomare, G. Cascarano, C. Giacobazzo, A. Guagliardi, M. C. Burla, G. Polidori, and M. Camalli, *J. Appl. Cryst.* **27**, 435 (1994).
- [25] P. Parois, R. I. Cooper, and A. L. Thompson, *Chem. Central J.* **9**, 30 (2015).
- [26] P. W. Betteridge, J. R. Carruthers, R. I. Cooper, K. Prout, and D. J. Watkin, *J. Appl. Crystallogr.* **36**, 1487 (2003).
- [27] R. I. Cooper, A. L. Thompson, and D. J. Watkin, *J. Appl. Crystallogr.* **43**, 1100 (2010).
- [28] A. L. Spek, *J. Appl. Crystallogr.* **36**, 7 (2003).
- [29] S. Blundell, *Magnetism in Condensed Matter* (Oxford University Press, Oxford, England, 2001).
- [30] E. Bellido, P. González-Monje, A. Repollés, M. Jenkins, J. Sesé, D. Drung, T. Schurig, K. Awaga, F. Luis, and D. Ruiz-Molina, *Nanoscale* **5**, 12565 (2013).
- [31] G. Tosi, F. A. Mohiyaddin, H. Huebl, and A. Morello, *AIP Adv.* **4**, 087122 (2014).
- [32] M. Jenkins, T. Hümmel, M. José Martínez-Pérez, J. García-Ripoll, D. Zueco, and F. Luis, *New J. Phys.* **15**, 095007 (2013).
- [33] A. Prokhorov and V. Fedorov, *Sov. Phys. JETP* **16**, 1489 (1963).
- [34] G. B. Teitel'baum, É. G. Kharakhash'yan, S. Y. Khlebnikov, and A. G. Zenin, *JETP Letters* **34**, 555 (1981).
- [35] D. I. Schuster, A. P. Sears, E. Ginossar, L. DiCarlo, L. Frunzio, J. J. L. Morton, H. Wu, G. A. D. Briggs, B. B. Buckley, D. D. Awschalom, and R. J. Schoelkopf, *Phys. Rev. Lett.* **105**, 140501 (2010).
- [36] E. Abe, H. Wu, A. Ardavan, and J. J. L. Morton, *Appl. Phys. Lett.* **98**, 251108 (2011).
- [37] A. Ghirri, C. Bonizzoni, D. Gerace, S. Sanna, A. Cassinese, and M. Affronte, *Appl. Phys. Lett.* **106**, 184101 (2015).
- [38] A. A. Clerk, M. H. Devoret, S. M. Girvin, F. Marquardt, and R. J. Schoelkopf, *Rev. Mod. Phys.* **82**, 1155 (2010).
- [39] C. W. Zollitsch, K. Mueller, D. P. Franke, S. T. B. Goennenwein, M. S. Brandt, R. Gross, and H. Huebl, *Appl. Phys. Lett.* **107**, 142105 (2015).
- [40] K. Katsumata, *J. Phys. Condens. Matter* **12**, R589 (2000).
- [41] T. Nagamiya, K. Yosida, and R. Kubo, *Adv. Phys.* **4**, 1 (1955).
- [42] J. Magariño, J. Tuchendler, and J. Renard, *Solid State Commun.* **26**, 721 (1978).
- [43] A. Kessel, B. M. Kozyrev, E. G. Kharakhash'yan, S. Y. Khlebnikov, and S. Z. Shakirov, *JETP Lett.* **17**, 453 (1973).
- [44] M. Oshikawa and I. Affleck, *Phys. Rev. B* **65**, 134410 (2002).
- [45] K. Nagata and Y. Tazuke, *J. Phys. Soc. Jpn.* **32**, 337 (1972).
- [46] Y. Maeda and M. Oshikawa, *J. Phys. Soc. Jpn.* **74**, 283 (2005).
- [47] M. E. Fisher, *Am. J. Phys.* **32**, 343 (1964).

SUPPLEMENTARY MATERIAL

Strong coupling of microwave photons to antiferromagnetic fluctuations in an organic magnet

Matthias Mergenthaler,^{1,2,*} Junjie Liu,¹ Jennifer J. Le Roy,¹ Natalia Ares,¹ Amber L. Thompson,³ Lapo Bogani,¹ Fernando Luis,⁴ Stephen J. Blundell,² Tom Lancaster,⁵ Arzhang Ardavan,² G. Andrew D. Briggs,¹ Peter J. Leek,² and Edward A. Laird^{1,†}

¹*Department of Materials, University of Oxford,
Oxford OX1 3PH, United Kingdom*

²*Clarendon Laboratory, Department of Physics,
University of Oxford, Oxford OX1 3PU, United Kingdom*
³*Chemical Crystallography, Chemistry Research Laboratory,
University of Oxford, Oxford OX1 3TA, United Kingdom*

⁴*Instituto de Ciencia de Materiales de Aragón
(CSIC-U. de Zaragoza), 50009 Zaragoza, Spain*

⁵*Durham University, Centre for Materials Physics,
Durham, DH1 3LE, United Kingdom*

(Dated: August 8, 2017)

* matthias.mergenthaler@materials.ox.ac.uk

† edward.laird@materials.ox.ac.uk

I. EXPERIMENTAL SECTION

A. Characterization of the resonator

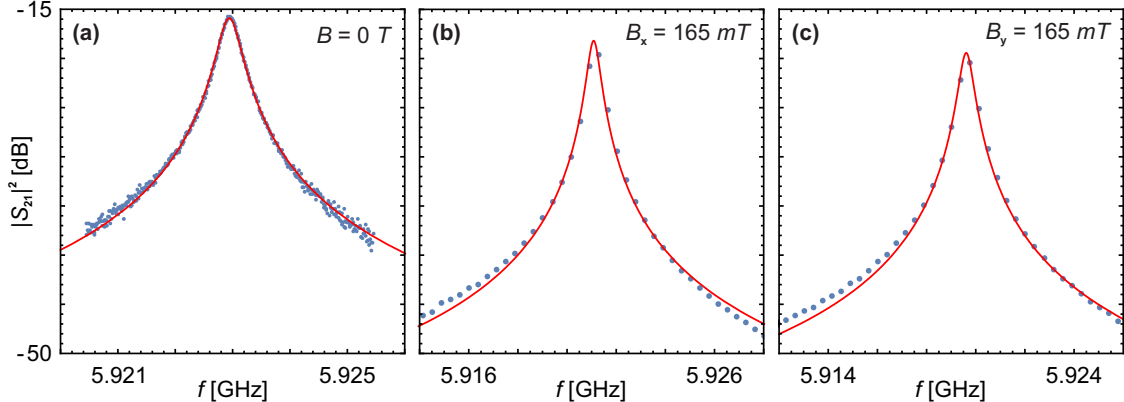


Figure S1. Points: Microwave transmission of the resonator at different magnetic field strengths and orientations. Lines: fits to Eq. (S1), with fit parameters listed in Tab. S1.

To extract the frequency and loaded quality factor Q_L of the resonator after attaching Crystal I, the measured transmission $|S_{21}(\omega)|^2$ was fitted according to

$$|S_{21}(\omega)|^2 = A_0 \frac{\kappa^2}{(\omega - \omega_0)^2 + \kappa^2}, \quad (\text{S1})$$

where the fit parameters are the amplitude A_0 , the resonance frequency $\omega_0/2\pi = f_0$ and the linewidth $2\kappa \equiv \omega_0/Q_L$. Figure S2 shows fits at zero magnetic field and in fields of 165 mT applied along x and y . The field was chosen to approach the spin resonance magnetic field, but far enough below it that the hybridization has still no influence on the resonance frequency. Table S1 shows the extracted fit parameters.

	B^{ext}	f_0	$\kappa/2\pi$	Q_L
-	0 T	5.923 GHz	195 kHz	15200
x	165 mT	5.921 GHz	251 kHz	11800
y	165 mT	5.919 GHz	283 kHz	10500

Table S1. Parameters extracted from Fig. S1

B. Growth and structure of the crystal

All reagents including 2,2-Diphenyl-1-picrylhydrazyl (DPPH; CAS: 1898-66-4), n-hexane, (99+%), and toluene, (99+%), were purchased from Sigma Aldrich or Fisher Scientific and used without further purification. Low temperature X-ray diffraction data were collected from Crystal II using an Oxford Diffraction (Rigaku) SuperNova diffractometer. Data were reduced using CrysAlisPro and solved using SIR92 [S1] within the CRYSTALS suite

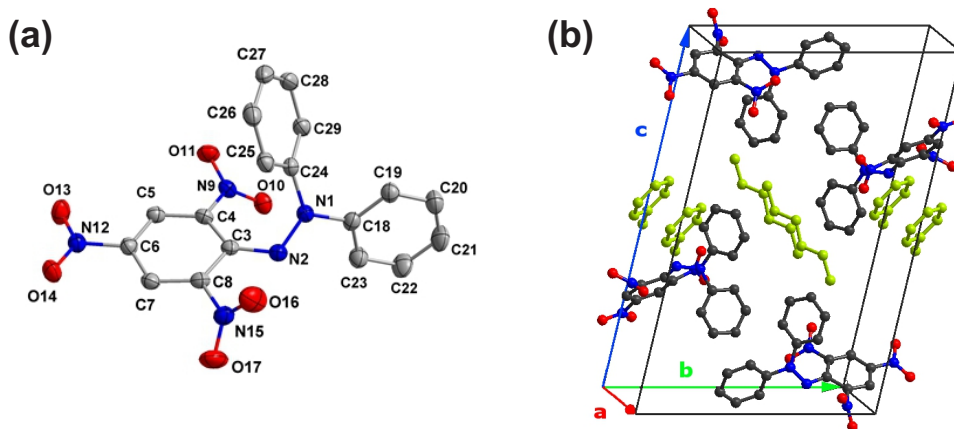


Figure S2. (a) Molecular structure of DPPH with displacement ellipsoids drawn at 50% probability. Color code: carbon (gray), oxygen (red), nitrogen (blue), hydrogen not shown. (b) Unit cell of the measured crystals containing four DPPH molecules, one hexane, and one toluene molecule per cell, with the latter two shown in green. The toluene exhibits crystallographic disorder (not shown). Lattice vectors \mathbf{a} , \mathbf{b} , \mathbf{c} are marked. Lattice constants are $|\mathbf{a}| = 7.4 \text{ \AA}$, $|\mathbf{b}| = 13.5 \text{ \AA}$, $|\mathbf{c}| = 21.7 \text{ \AA}$.

[S2, S3]. The structure was refined using full-matrix least-squares with CRYSTALS to give the unit cell shown in Fig. [S2]. Disordered solvent in each unit cell was modelled as one toluene molecule. In general, hydrogen atoms were visible in the difference map and refined separately using soft restraints prior to inclusion in the final refinement using a riding model [S4]. There was no evidence of protonation of the central nitrogen atom in each molecule (N2 in Fig. [S2]). Comparison of the final refinement with that generated using PLATON/SQUEEZE [S5] suggested that the disordered toluene model was a good fit to the electron density. Full refinement details are given in the Supporting Information (CIF file). Crystallographic data (excluding structure factors) have been deposited with the Cambridge Crystallographic Data Centre (CCDC 1475359) and will be available via http://www.ccdc.cam.ac.uk/data_request/cif.

C. Bulk susceptibility measurements

1. High temperature measurements

Magnetization $M(T)$ was measured as a function of temperature (and converted to susceptibility by the relation $\chi(T) = M(T)/H$) using a Quantum Design MPMS 7 T SQUID. Polycrystalline samples of DPPH were loaded into gelatin capsules, mounted in a plastic drinking straw, and affixed to the end of a stainless steel/brass rod. The sample was cooled from 300 K to 1.8 K.

Results are shown in Fig. [S3]. Near room temperature the product χT is constant at a value 0.37 emu/K mol Oe, as expected for a paramagnet with $S = 1/2$ and $g = 2.0$ [S6, Eq. (A.8)]. Below ~ 100 K, the susceptibility decreases, consistent with antiferromagnetic spin interactions. The additional structure in the data observed on cooling may reflect different values of the intermolecular exchange along different crystallographic directions, not included in the chain model in the main text.

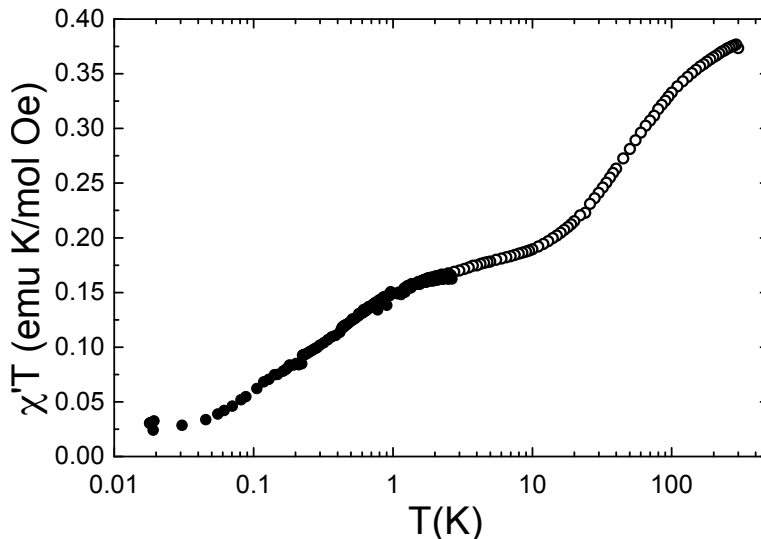


Figure S3. Magnetic susceptibility of a polycrystalline sample of DPPH. Data is plotted as the χT product, which was corrected for the diamagnetic background. High- and low-temperature measurements are marked with open and filled circles respectively.

2. Low temperature measurements

To measure susceptibility below 1.8 K, we used a 30 μm micro-SQUID susceptometer [S7]. Polycrystalline samples of DPPH were attached with Apiezon N grease to a SQUID loop. The sample was cooled from 3 K to 16 mK in a dilution refrigerator and an AC magnetic field of amplitude 0.25 Oe was applied with its frequency varied from 0.3 Hz to 200 kHz.

Figure [S4] shows representative results of the in-phase, χ' , and out-of-phase, χ'' , component of the susceptibility χ . Below ~ 1.7 K the product $\chi'T$ is decreasing, which is consistent with antiferromagnetic interactions. However, no evidence of a phase transition (in the form of a peak in $\chi'(T)$) could be detected, indicating that any transition from PM to AFM occurs below 16 mK. From the peak in $\chi''(T)$ it is evident that there is an onset of slow relaxation below 150 mK.

D. Muon spin relaxation measurements

To further exclude long-range magnetic ordering we carried out muon-spin relaxation measurements down to $T = 19$ mK. Measurements were performed at the Swiss Muon Source, Paul Scherrer Institute using the LTF instrument. Roughly 100 mg of polycrystalline DPPH was attached with vacuum grease to a thin silver foil, which in turn was attached to a silver plate mounted on the cold finger of the dilution refrigerator. In a μ^+ SR experiment spin polarized muons are implanted into the sample. The measured quantity is the asymmetry $A(t)$, which is proportional to the spin polarization of the muon ensemble.

This asymmetry at each temperature (Fig. [S5]) shows a broadly Gaussian relaxation, which we attribute to the magnetism of randomly oriented quasistatic nuclear spins. Significantly, the spectra are quite temperature independent up to $T = 0.8$ K and we do not

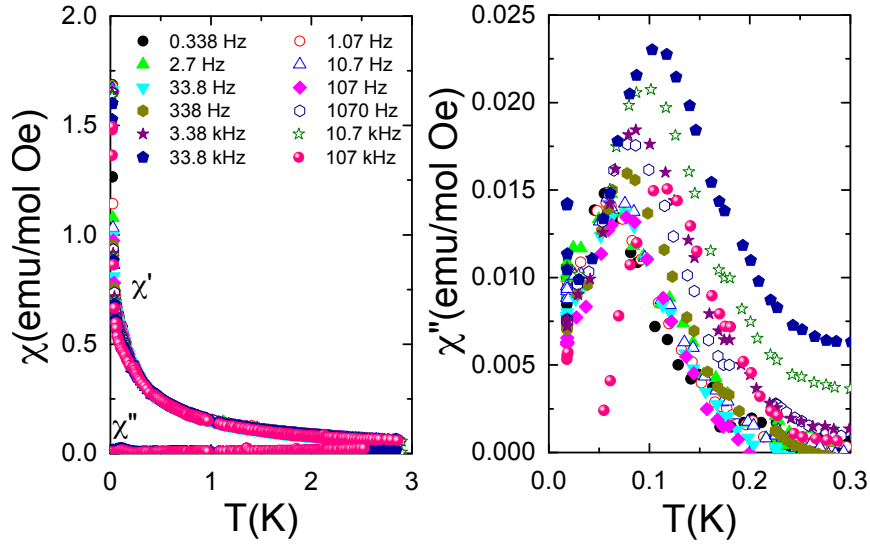


Figure S4. Magnetic susceptibility of a polycrystalline sample of DPPH for $T \leq 3$ K, measured with twelve different ac-magnetic field frequencies. Data is shown for the in-phase, χ' , and out-of-phase, χ'' , component.

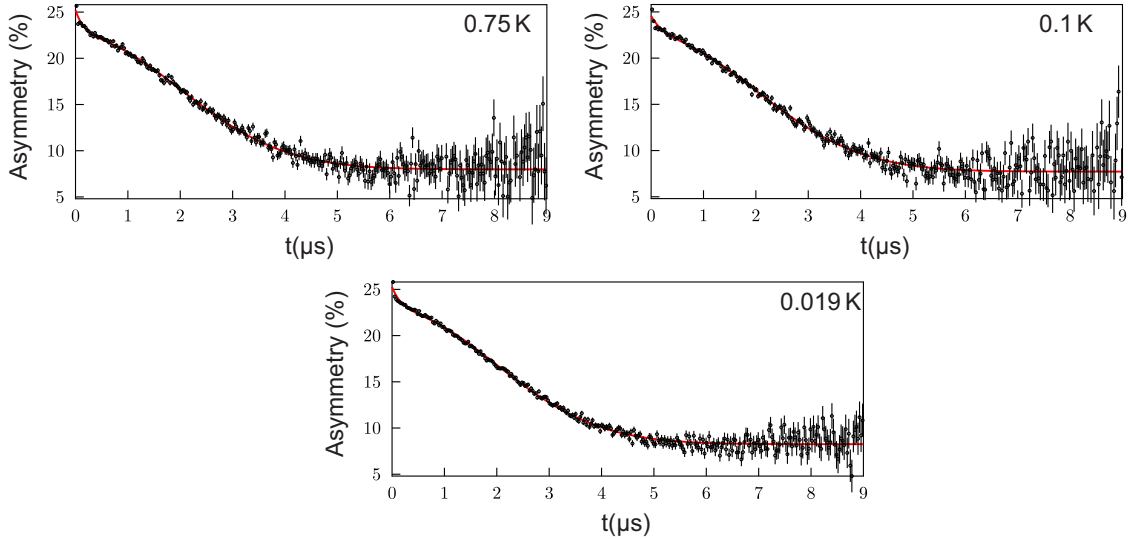


Figure S5. Example asymmetry as a function of time for a polycrystalline sample of DPPH, measured at three temperatures

observe any spontaneous oscillations in the asymmetry or a shift in the baseline that might be expected for a transition to a regime of long range magnetic order. We therefore conclude that the system is magnetically disordered down to $T = 19$ mK, with electronic moments fluctuating outside the muon time window, causing them to be motionally narrowed from the spectra.

E. Measurement of a second crystal

The measurements of Fig. 3(a)-(b) and Fig. 4(a) in the main text were rerun with a second sample (Crystal II) from a different growth batch, which used a newly opened bottle of DPPH powder precursor. The measurements and the extracted parameters are similar to the results presented in the main text. Following these measurements, X-ray characterization was performed on this crystal, confirming the structure of Fig. S2.

Figure S6 shows measurements and fits similar to Fig. 2 of the main text. Extracted parameters are given in Table SII. The magnetic resonance field is slightly lower than in the main text, consistent with the lower cavity frequency (presumably because Crystal II was slightly larger and acted as a dielectric load). Measurements similar to Fig. 3 of the main text are shown in Fig. S6, again with similar results. The extracted anisotropy of B_{MR} and the spin-flip field are the same as in the main text, to within 4 %, confirming reproducibility.

T (K)	Axis	B_{MR} (mT)	$g_{\text{eff}}/2\pi$ (MHz)
4	x	208.36 ± 0.02	17.01 ± 0.1
4	y	209.32 ± 0.02	12.75 ± 0.1
0.015	x	200.6 ± 0.01	38.04 ± 0.1
0.015	y	210.86 ± 0.06	29.59 ± 0.3

Table SII. Resonance parameters extracted from Fig. S6 for different temperatures and magnetic field orientations.

To confirm that the anisotropy is associated with the crystal rather than the resonator we repeat the low- T fundamental-mode measurement of Fig. S7(a) after rotating the crystal by 90° in the xy plane. The data shows the expected shift (Fig. S8(a)), confirming that the anisotropy arises from the crystal structure rather than e.g. screening by the resonator. We also measure the crystal in a configuration rotated by approximately 90° in yz in order to

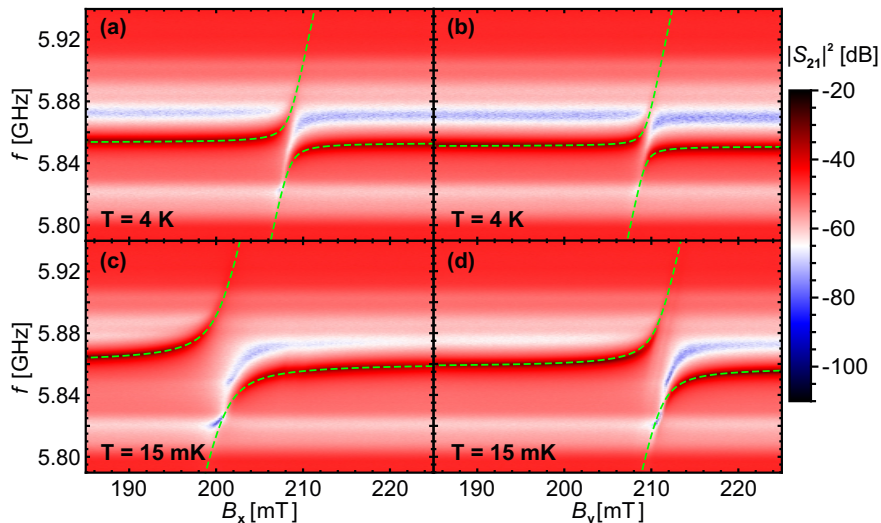


Figure S6. Transmission as a function of external magnetic field $B_{x,y}$ and resonator probe frequency f , measured at two different temperatures using Crystal II. Superimposed on each panel are fits (dashed lines) using Eq. (1) from the main text.

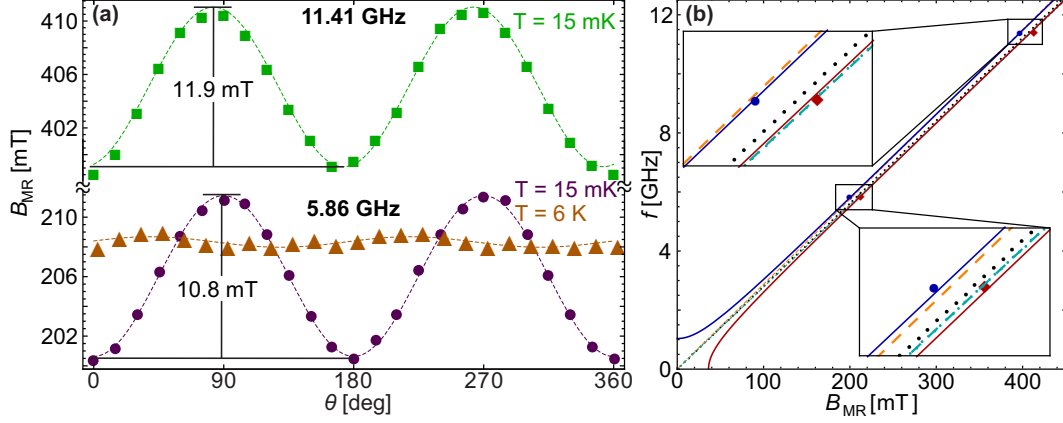


Figure S7. As Fig. 3 of the main text, for measurements on Crystal II. (a) Resonance magnetic field B_{MR} as function of field angle θ at different cavity modes and temperatures, with fits. (b) Plot of the MR frequency as a function of resonance magnetic field, fitted with paramagnetic dispersion relation as in main text (dashed/dotted/dot-dashed lines) and antiferromagnetic dispersion relation (main text Eq. 3, solid lines).

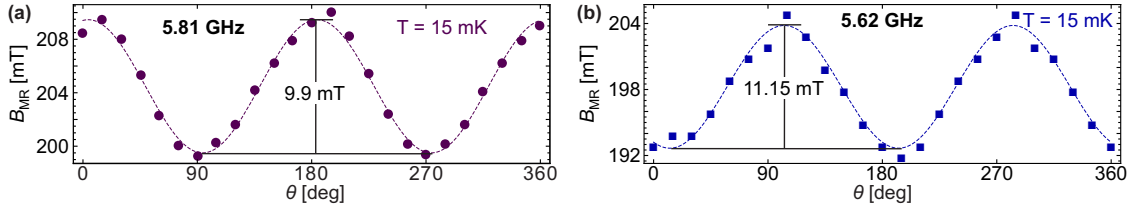


Figure S8. (a) Resonance magnetic field B_{MR} as function of field angle θ , after the crystal has been rotated by 90° in the xy plane. Data is measured near the fundamental mode and at $T = 15$ mK. Compared to Fig. S7 (a) the trace is shifted by 90° , as expected due to the crystal rotation. (b) Equivalent data after rotation by $\sim 90^\circ$ in the yz plane from configuration of Fig. S7.

map the anisotropy axis in three dimensions. The angle dependence in this configuration is shown in Fig. S8(b). Although the anticrossing was harder to identify for some field angles in this configuration, the estimated resonance positions show the same sinusoidal dependence as for Fig. S7(a) and indicate uniaxial behaviour with anisotropy axis along x in Fig. 1 main text.

The temperature dependence of B_{MR} is similar as for Crystal I (Fig. S9). Here the temperature below which the spins in the crystal fail to thermalize is estimated to be around $T \approx 75$ mK. A similar value is also estimated from B_{MR} at the first harmonic (Fig. S9 inset). Performing the same analysis as in Fig. 4 of the main text, we extract for the one-dimensional model similar values $J/k_B = 235$ mK and $J^A/k_B = -7.5$ mK.

II. MODELLING THE TEMPERATURE-DEPENDENT FREQUENCY SHIFT

In this section, we explain the model leading to the fits in Fig. 4 of the main text. We use the spin chain Hamiltonian Eq. (4) of the main text.

Because exchange interaction between spins leads to hybridization of the eigenstates, the

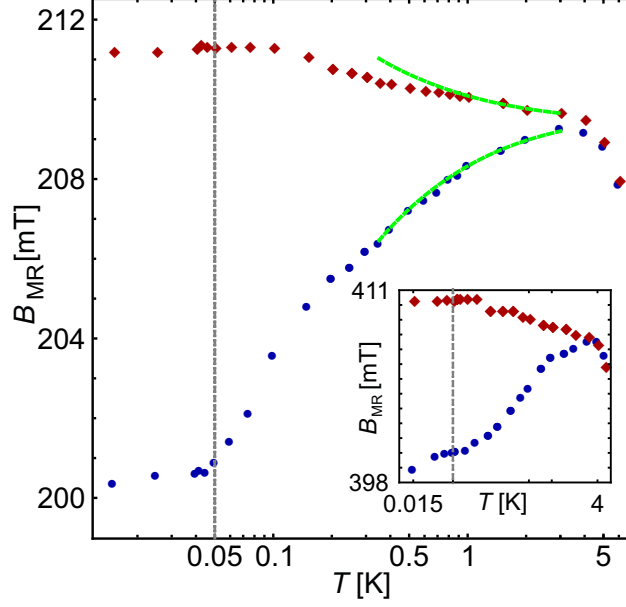


Figure S9. Data and analysis similar to Fig. 4(a) of the main text, for Crystal II. Main panel: temperature dependence of B_{MR} (points) with model (lines) for fundamental mode of the resonator. Inset: same data for first harmonic mode.

magnetic resonance frequency in general shifts away from the paramagnetic value as the crystal is cooled into its antiferromagnetic phase. At high temperature, spin correlations are negligible and the magnetic resonance frequency is given by the single-spin Zeeman splitting. At lower temperatures, as nearby spins become correlated, there is an exchange shift. In the antiferromagnetic phase, the magnetic resonance frequency corresponds to the energy of a long-wavelength magnon.

For this one-dimensional model, the shift calculated in perturbation theory (Eq. (5) of the main text) was evaluated in Ref. [S8]:

$$\delta f_{\parallel} = -4 \frac{J^A}{h} \frac{\langle S_i^x S_{i+1}^x - S_i^y S_{i+1}^y \rangle}{\langle S^x \rangle / N} \quad \text{for } \mathbf{B} \text{ along } x \quad (\text{S2})$$

$$\delta f_{\perp} = 2 \frac{J^A}{h} \frac{\langle S_i^y S_{i+1}^y - S_i^x S_{i+1}^x \rangle}{\langle S^y \rangle / N} \quad \text{for } \mathbf{B} \text{ along } y. \quad (\text{S3})$$

where N is the number of spins in the crystal. Thus, given the anisotropic exchange strength J^A , the measured frequency shift is a direct measure of temperature-dependent correlation functions.

Extracting the exchange parameters J and J^A from data requires a knowledge of the correlation functions in Eq. (S2-S3). Even in this comparatively simple model, these are not known. However, we can estimate them following Ref. [S8] by making two additional assumptions:

1. We rely on the smallness of \mathcal{H}' compared to \mathcal{H}^0 to approximate

$$\langle \dots \rangle \approx \langle \dots \rangle_0. \quad (\text{S4})$$

In other words, the thermal expectation values in Eqs. (S2-S3), which are determined by the entire Hamiltonian \mathcal{H} , can be replaced by thermal expectation values $\langle \dots \rangle_0$ under the unperturbed Hamiltonian \mathcal{H}^0 .

2. We use a classical spin model in which the quantum mechanical spin operators are replaced by classical vectors [S9].

Because of the rotational symmetry of \mathcal{H}^0 , assumption (1) immediately leads to the equivalence of the two sets of expectation values in Eqs. (S2-S3), implying that the frequency shifts along the two directions should differ by a factor -2. This is in fair agreement with the data of Fig. 4, supporting this model.

Assumption (2) reflects the correspondence of quantum and classical pictures at high temperature. It allows the expectation values to be evaluated by expanding two-spin correlators at finite field in terms of higher-order correlators at zero field [S8]. The result is (to lowest order in J^A/J):

$$\delta f_{\parallel} = \frac{2J^A g \mu_B B}{5hJv} \left\{ \frac{2 + uv}{1 - u^2} - \frac{2}{3v} \right\} \quad (\text{S5})$$

$$\delta f_{\perp} = -\frac{\delta f_{\parallel}}{2}, \quad (\text{S6})$$

expressed in terms of dimensionless parameters

$$u(J, T) \equiv \coth w - 1/w \quad (\text{S7})$$

$$v(J, T) \equiv -1/w \quad (\text{S8})$$

$$w \equiv \frac{2JS(S+1)}{k_B T}. \quad (\text{S9})$$

The fit curves in Fig. 4 derived from Eqs. (S5-S6) are then:

$$B_{\text{MR}}(\parallel) = \frac{h(f_0 + \delta f_{\parallel})}{g\mu_B} \quad (\text{S10})$$

$$B_{\text{MR}}(\perp) = \frac{h(f_0 + \delta f_{\perp})}{g\mu_B} \quad (\text{S11})$$

with $g = 2$. The failure of the fits at low temperature presumably reflects the increasing importance of quantum correlations, neglected by assumption (2) above, or of interactions beyond one dimension. Thus, to the extent that our spin-chain approximation is correct, the data of Fig. 4 provide a measurement of the spin correlation function that is more accurate than provided by the calculation relying on assumption (2) above.

III. COLLECTIVE COUPLING PARAMETERS

A. Single spin coupling rate

The single spin-photon coupling rate, g_s , is proportional to the vacuum magnetic field B_{vac} , of the resonator [S10]

$$g_s = \frac{g\mu_B B_{\text{vac}}}{4\hbar}, \quad (\text{S12})$$

where $g = 2.0037$ is the Landé g-factor of DPPH, μ_B the Bohr magneton, and \hbar the Planck constant. From the resonator's geometry [S10], we approximate

$$B_{\text{vac}} \approx \frac{\mu_0 I_{\text{vac}}}{2(w + 2s)}, \quad (\text{S13})$$

where μ_0 is the vacuum magnetic permeability, I_{vac} the zero-point current in the resonator, and w and s the center conductor width and spacing from the lateral groundplanes, respectively. The zero-point current of a resonator with characteristic impedance Z_0 and resonance frequency f_0 is given by [S10]

$$I_{\text{vac}} = \pi f_0 \sqrt{\frac{h}{Z_0}} \quad (\text{S14})$$

For our resonator with $Z_0 = 50 \Omega$, $f_0 = 5.921 \text{ GHz}$, $w = 50 \mu\text{m}$ and $s = 5.3 \mu\text{m}$ this yields $B_{\text{vac}} \approx 7 \times 10^{-10} \text{ T}$ and therefore $g_s/2\pi \approx 5 \text{ Hz}$.

B. Number of coupled radicals in crystal

The DPPH crystal was measured to have a length of $365 \mu\text{m}$. The effective coupled width of the crystal is assumed to be $w + 2s = 60.6 \mu\text{m}$. Additionally, a penetration depth of the vacuum magnetic field of $4 \mu\text{m}$ is assumed [S11]. This results in a coupled crystal volume of $V = 1 \times 10^{-7} \text{ cm}^3$. Taking the density of molecules from the diffraction data (Fig. S2) as $\rho_V \sim 2 \times 10^{21} \text{ cm}^{-3}$, then the number of coupled radicals in our crystal is $N = \rho_V V \sim 1.7 \times 10^{14}$.

-
- [S1] A. Altomare, G. Cascarano, C. Giacovazzo, A. Guagliardi, M. C. Burla, G. Polidori, and M. Camalli, *Journal of Applied Crystallography* **27**, 435 (1994).
- [S2] P. Parois, R. I. Cooper, and A. L. Thompson, *Chemistry Central journal* **9**, 30 (2015).
- [S3] P. W. Betteridge, J. R. Carruthers, R. I. Cooper, K. Prout, and D. J. Watkin, *Journal of Applied Crystallography* **36**, 1487 (2003).
- [S4] R. I. Cooper, A. L. Thompson, and D. J. Watkin, *Journal of Applied Crystallography* **43**, 1100 (2010).
- [S5] A. L. Spek, *Journal of Applied Crystallography* **36**, 7 (2003).
- [S6] S. Blundell, *Magnetism in Condensed Matter* (Oxford University Press, 2001).
- [S7] E. Bellido, P. González-Monje, A. Repollés, M. Jenkins, J. Sesé, D. Drung, T. Schurig, K. Awaga, F. Luis, and D. Ruiz-Molina, *Nanoscale* **5**, 12565 (2013).
- [S8] K. Nagata and Y. Tazuke, *Journal of the Physical Society of Japan* **32**, 337 (1972).
- [S9] M. E. Fisher, *American Journal of Physics* **32**, 343 (1964).
- [S10] G. Tosi, F. A. Mohiyaddin, H. Huebl, and A. Morello, *AIP Advances* **4**, 087122 (2014).
- [S11] M. Jenkins, T. Hümmel, M. José Martínez-Pérez, J. García-Ripoll, D. Zueco, and F. Luis, *New Journal of Physics* **15**, 95007 (2013).